https://doi.org/10.5194/egusphere-2026-115
Preprint. Discussion started: 3 February 2026

Probabilities of Detection of Methane Plumes by Remote Sensing and Implications for Inferred Emissions Distributions

Ethan Manninen[1], Apisada Chulakadabba[1,2], Maryann Sargent[1], Zhan Zhang[1], Harshil Kamdar[3], Jack Warren[4], Sébastien Roche[1,4,5], Christopher Chan Miller[1,4,5], Ethan Kyzivat[1], Joshua Benmergui[1,4], Jasna Pittman[1], Eleanor Walker[1], Jacob Bushey[1], Jenna Samra[5], Jacob Hawthorne[5], Bingkun Luo[5], Maya Nasr[1,5], Kang Sun[6], Jonathan Franklin[1], Xiong Liu[5], Jia Chen[2], and Steven Wofsy[1]

[1]Harvard University School of Engineering and Applied Sciences, Cambridge, MA, USA
[2]School of Computation, Information and Technology, Technischen Universität München, Munich, Germany
[3]Insight M, Sunnyvale, CA USA 94085
[4]Environmental Defense Fund, Washington DC, USA
[5]Center for Astrophysics, Harvard and Smithsonian, Cambridge, MA, USA
[6]Research and Education in Energy, Environment, and Water Institute, University at Buffalo, Buffalo, NY, USA

Correspondence: Steven Wofsy (wofsy@g.harvard.edu)

Abstract. Strategies for mitigating methane emissions rely on understanding the underlying drivers of methane losses to the atmosphere. Observations of methane plumes emerging from point sources, combined with correct statistical interpretation, can provide key information. In this work, we examine a critical parameter, the probability of detection of a plume. For a given observing system, probability of detection is affected by the properties of the sensor, plume detection algorithm, observing conditions, and emission rate of the source. We parameterize relevant aspects of remotely sensed scenes containing plumes using a nondimensional observability parameter that predicts probability of detection. Our probability of detection model is trained using simulated plumes to capture natural variability in different meteorological conditions, and validated with data from controlled release experiments. We model probability of detection for two airborne imaging spectrometer systems, MethaneAIR and Insight M LeakSurveyor™, and one high resolution satellite system, MethaneSAT. Monte Carlo simulations of emissions distributions implied by data from the extensive 2023 MAIRX campaign of MethaneAIR demonstrate the importance of an accurate probability of detection model, due to the heavy tailed emission distribution found in most oil and gas basins.

1 Introduction

Remotely sensed observations of methane (CH_4) plumes offer fundamental insight into the crucial climate challenge of methane emissions (Varon et al. (2018)). To understand the underlying drivers of CH_4 emissions, we need to characterize the contributions of different emission rates and processes to total CH_4 emissions. A key piece of information needed for this assessment is the probability of detection (P_d) of a CH_4 plume with different sensors, under different observing conditions, and using different detection algorithms (Conrad et al. (2023)).

https://doi.org/10.5194/egusphere-2026-115
Preprint. Discussion started: 3 February 2026

We set out to answer the question: "How can we integrate plume observations by different remote sensing systems to assess the emission rate dependent distribution of point sources and their contributions to total emissions?" We develop a generalized approach to account for the factors that affect P_d, and apply it to observations by MethaneAIR, MethaneSAT, and Insight M LeakSurveyor™. We utilize data from controlled release experiments, extended with image processing techniques, and supplemented with simulated plumes. Our approach enables us to model systems lacking available controlled release data such as MethaneSAT. Finally, we demonstrate the effect of the P_d term on emissions distribution analyses of observations of the Permian Basin.

Previous work defines P_d as a function of emission rate scaled by wind speed, assuming unobstructed transport of CH_4 from the source (Sherwin et al. (2021)). Conrad et al. (2023) fit continuous P_d curves to controlled release experiment data collected by several sensors, using dimensional parameters unique to each system. This approach is limited by the availibility of controlled release data, which only capture a subset of the variability in observing conditions found in nature. The approach we use here, extending the training data with simulated plumes, has been used for plume detection algorithms (Rouet-Leduc and Hulbert (2024)) and for P_d models (preprint: Roger et al. (2025)). If they are available, coincident observations by higher threshold and lower threshold observing systems can be used to estimate P_d for the lower threshold system (Ayasse et al. (2024)). Ayasse et al. (2024) also use their P_d estimate to weight an emissions distribution recovered from satellite observations.

2 Methods

2.1 Desiderata of a Probability of Detection Model

A useful model of probability of detection allows integration of plume counts from different scenes and observing systems. Study of P_d is in service of interpreting plume counts. Different observing systems have different nominal pixel areas and gas sensitivities. Scenes from the same observing system vary in observing conditions, which affect the ability to detect plumes (Conrad et al. (2023)). These include wind speed, aircraft altitude, solar zenith angle, surface albedo, and aerosol optical depth. Additionally, there are many algorithms applied to XCH_4 scenes to detect plumes. An effective P_d model enables intercomparison of XCH_4 scenes from different observing systems by accounting for: 1) the sensors' XCH_4 sensitivity and spatial resolution 2) the skill of plume detection algorithms 3) the observing conditions of each scene.

Following Conrad et al. (2023), we model P_d with a combination of an inverse link function $F : \mathbb{R} \rightarrow [0, 1]$ and a predictor function $g : \mathbf{x} \rightarrow \mathbb{R}$:

$$P_d = F(g(\mathbf{x}, \boldsymbol{\phi}), \boldsymbol{\theta}) \tag{1}$$

where $\mathbf{x}$ is the set of variables that affect P_d and $\boldsymbol{\phi}$ and $\boldsymbol{\theta}$ are the coefficients for F and g. The predictor function g parameterizes the factors that affect plume observability, while the inverse link function $F : \mathbb{R} \rightarrow [0, 1]$ converts g to a probability. They tested a variety of functional forms for F and g and used Akaike Information Criterion (AIC) ranking to select the optimal model for each observing system in each controlled release experiment (Akaike (1992)). Selecting from many different functional forms yields a close P_d fit for each controlled release experiment. However, when trying to extend the P_d model from the controlled

https://doi.org/10.5194/egusphere-2026-115
Preprint. Discussion started: 3 February 2026

release to analysis of observations, this close fit may be a detriment if the controlled release observations are not representative. In service of our goal of analyzing plume observations from multiple scenes and observing systems, we used a single pair of forms for the predictor function g and inverse link function F, similar to Bruno et al. (2024).

Bruno et al. (2024) used a dimensionless predictor function of emission rate, wind speed, and pixelwise column concentration uncertainty they call *Observability*. In Bruno et al. (2024), Observability is combined with a sigmoid inverse link functional form. We also use a nondimensional predictor function and sigmoid inverse link function (Section 2.6). To train these P_d models, we use Weather Research Forecasting, Large Eddy Simulation (WRF-LES) plumes (Section 2.4) and controlled release data for validation (Section 2.3). We use these P_d models for an emissions distribution analysis of a comprehensive North American observation campaign by MethaneAIR (Section 2.7,3.3).

2.2 Imaging Spectrometers

We studied three imaging spectrometers: MethaneAIR, MethaneSAT, and Insight M's LeakSurveyor™. The MethaneAIR observing system is an imaging spectrometer flown at a 12 km nominal observing altitude above ground level Staebell et al. (2021). At this altitude, the footprint of a single XCH_4 sounding is 5m x 25m. MethaneAIR flew the MAIR (summer 2021) and MAIR-E (summer 2022) research campaigns to develop emissions quantification algorithms. The MAIRX campaign quantified emissions from basins across North America in May-October 2023. There have been two MethaneAIR aircraft: the NSF Gulfstream GV operated by NCAR used for MAIR and MAIR-E, and a Learjet Model 35 operated by IO Aerospace for MAIRX. The MethaneAIR spectral retrieval is detailed in Conway et al. (2024). XCH_4 is inverted from retrieved backscattered solar spectra following the XCO_2 proxy method described by Chan Miller et al. (2024), with the prior XCO_2 derived from profiles generated using the GINPUT algorithm (Laughner et al. (2023)).

MethaneAIR is the airborne precursor for the MethaneSAT mission. MethaneSAT is a satellite regional XCH_4 mapper that can also detect CH_4 plumes. It was launched in March 2024, and made observations at ∼590 km observing altitude until the satellite lost power in June, 2025. MethaneSAT observations have nominal pixel dimensions of 110m x 450m at nadir, with a wider swath of ∼200km compared to MethaneAIR's 5km. Insight M LeakSurveyor™ is an imaging spectrometer flown on light aircraft at observation altitudes of 370-900m. At 370m, this observation altitude results in a smaller pixel area of $\sim 5m^2$, at the cost of a narrower swath width. It has proprietary spectroscopy and retrieval algorithms. Insight M was previously known as "Kairos Aerospace", the name under which LeakSurveyor™ data were analyzed in Conrad et al. (2023) and Sherwin et al. (2024).

2.3 Controlled Release Experiments

In a controlled release experiment, research teams attempt to detect and quantify plumes, usually blinded to the emission rate (Sherwin et al. (2021)). Both airborne and satellite observing systems have been characterized via controlled release (Sherwin et al. (2023)). MethaneAIR flew controlled release experiments in 2021 in the Permian Basin, Texas, USA and in 2022 in central Arizona, USA (Chulakadabba et al. (2023); El Abbadi et al. (2024)). LeakSurveyor™ also participated in the 2022 experiment (Sherwin et al. (2023); El Abbadi et al. (2024)). For these two experiments, the research teams knew the emission

https://doi.org/10.5194/egusphere-2026-115
Preprint. Discussion started: 3 February 2026

location but not whether it was emitting for each overpass. LeakSurveyor™ flew at 900 m above ground level for the 2021 experiment, but at 370-540 m observing altitude for the 2022 experiment (Conrad et al. (2023); El Abbadi et al. (2024)). Controlled release experiments were attempted for MethaneSAT prior to its loss, but coordinating overpasses with release durations failed on available trials.

2.4 Simulated Plumes

Data from controlled release experiments are valuable because they provide well constrained emission rates and windspeeds, which are needed to model P_d. These data are rare and expensive, with most experiments producing at most hundreds of observations. As a result, they only describe a subset of the natural variability in observing conditions. For example, the maximum observed wind speed in the 2021 and 2022 controlled release experiments was 3.3 m/s (Chulakadabba et al. (2023)). In the summer of 2023, MAIRX saw HRRR wind speeds up to 7.9 m/s. Additionally, controlled release experiments occur in a single location, which limits the variety of tested surface albedo and topography. The locations of potential emissions are also often known, affecting P_d.

To increase the data available to assess P_d, we generated simulated plumes using image processing methods to modify the properties of observed controlled release plumes. This resulted in a training set of ∼80,000 simulated scenes and a validation data set of ∼62,000 scenes derived from ∼40 controlled release overpasses. These plume simulations and image manipulations extend our analysis to wind conditions and emission rates that span the wider range of conditions observed in nature. In this way, effective simulation better represents reality than our limited observations of reality.

To generate artificial plumes, we used the WRF-LES model and image processing. WRF-LES effectively captures the stochastic behavior of plumes due to boundary layer turbulence Gaudet et al. (2017); Chulakadabba et al. (2023). To reduce computation times, we used an idealized version of WRF-LES, which uses a time invariant upwind boundary condition. Using idealized WRF-LES, we simulated plumes evolving under wind speeds between 0 and 15 m/s in the WRF model. To further extend the training scenes, we used image processing to change the emission rate, pixel area, and gas concentration noise of each idealized WRF-LES scene. First, we produced plumes of varying emission rates by scaling the XCH_4 of each pixel by the ratio of the original WRF-LES emission rate to the desired emission rate. This scaling relies on the linearity of CH_4 transport. Next, we aggregated pixels to vary their area. Finally, we added Gaussian noise. We observed a spatial correlation between adjacent pixels of .7 in MethaneAIR scenes, and maintained that level of spatial correlation in the simulated scenes. This process generated a training data set of ∼80,000 simulated plumes. Figure 1 shows examples of the simulated plumes with different parameters. We applied the same method of scaling noise and emission rate to controlled release scenes to create a more widely varying validation dataset. These scenes have varying emission rate, pixel area, and gas concentration noise, but wind speed cannot be changed without changing the shape of the plume. To train P_d models, we applied operational MethaneAIR and MethaneSAT plume detection algorithms to all of these simulations, as described in the next section.

https://doi.org/10.5194/egusphere-2026-115
Preprint. Discussion started: 3 February 2026

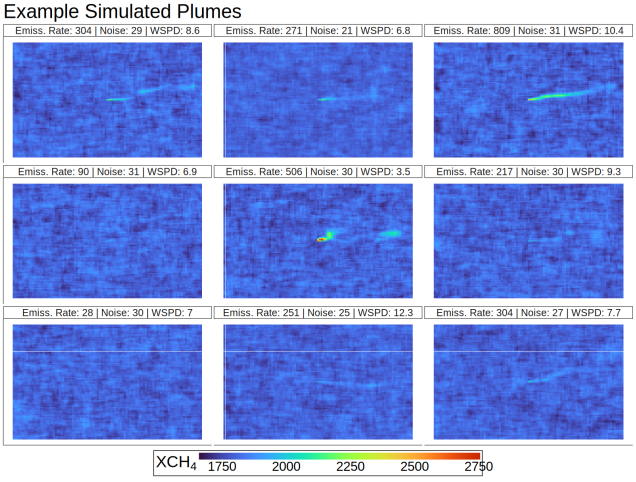

Figure 1. Example simulated plumes. Color represents XCH_4. Each plume has a different combination of emission rate (kg/hr), pixel area (m^2), gas concentration noise (ppb), and wind speed (m/s).

2.5 Detection Algorithms

We analyzed two plume detection algorithms used by MethaneAIR and MethaneSAT, the divergence integral and wavelet methods. The divergence integral method uses Gauss's theorem to measure the amount of CH_4 leaving a small area (Chulakadabba et al. (2023); Warren et al. (2024)). Adapted from medical imagery applications, the wavelet method isolates high frequency XCH_4 variation, interpreted as noise, and subtracts that structure from the observations. This leaves behind structured low frequency variation, interpreted as plumes (Hüpfel et al. (2021)).

We apply the plume detection algorithms to the training set of simulated plumes and recorded the successful and failed detections as binary outcomes. Here, plume detection is fully automated; there is no manual quality assurance step to identify false positives, which are not a focus of this study. We also analyze output from the Insight M algorithm used to detect plumes in LeakSurveyor scenes. Insight M provided the data required for our analysis from the 2022 Arizona controlled release experiment, including gas concentration noise, pixel area, and detection success. Their detection algorithm and controlled release scenes are not available to the public.

2.6 Logistic Regression on Parameterized Plume Observability

Following Bruno et al. (2024), we use a single log-linear form for g for all systems and scenes because it is simpler than using a different functional form for each observing system and experiment.

$$\text{Observability} \equiv g(q, a_p, \tilde{n}, u) = log\left(\frac{q}{\sqrt{a_p}\tilde{n}u}\right) \tag{2}$$

https://doi.org/10.5194/egusphere-2026-115
Preprint. Discussion started: 3 February 2026

Table 1. Variables and units used in equation 2.

Symbol	Name	Units
g	Observability (predictor function)	Dimensionless
q	Emission Rate†	ppb m^2 s^{-1}
a_p	Pixel Area	m^2
$\tilde{n}$	Gas Concentration Noise	ppb
u	Horizontal Wind Speed	ms^{-1}

†: Here ppb refers to the enhancement of the column mean dry mole fraction (plume excess XCH_4). To convert to kg/s, multiply q by $M_{air}/M_{CH_4} \cdot 10^{-9}/g \times P_{surf} \times (1 - XH_2O)$

Observability g parameterizes the observing conditions and observing system characteristics into a single dimensionless term. Variable names and units for Equation 2 can be found in Table 1. The lack of dimension enables ease of translation between observability space and relevant features like emission rate and wind speed. We expect the eddy scale wind speed to be the boundary of viability for the observability parameter. As such, this approach should not necessarily be applied to low wind night time conditions without further investigation. We further note that the observability parameterization is applicable to passive remote sensing systems, while active systems would require an additional scaling with the inverse square of observation altitude to account for power loss over distance. The observability link function is passed to the inverse function F, following Conrad et al. (2023). Differing from Conrad et al. (2023), and following Bruno et al. (2024), we do not use different functional forms for F for different systems and release experiments.

For fitting and validating P_d models, the emission rate q is known from a controlled release meter or prescribed when simulating the plume. For each scene, fitted P_d models predicted P_d for a range of emission rates. Pixel area is calculated from the XCH_4 scene. The gas concentration noise ($\tilde{n}$) contains noise contributions from the instrument as well as the observing conditions, including disturbances from upwind sources. For a given scene, $\tilde{n}$ is the standard deviation of the XCH_4 values of a "clean" portion of the scene. In this context, clean means that there is no variability from proximate emissions. Finding a clean portion of a scene can be done by visual inspection or by taking the pixels below a percentile cutoff. We collected the pixels below the 10th percentile. Clean portions of scenes can be found in many ways, but they are confirmed clean by checking that the XCH_4 values are normally distributed for the pixels selected. This means that clean XCH_4 pixels are unstructured, but unaffected by local emissions. Proximate emissions are a valid source of gas concentration noise— it is harder to identify a plume in a scene with many sources than a plume from an isolated source. In large scenes, there may be multiple gas concentration noise values, in which case a more accurate P_d may be calculated by considering subscenes. We used wind speed measured by the anemometer at the controlled release site (Chulakadabba et al. (2023)). To predict P_d with a fitted model for MAIRX scenes, we used the lowest-level High Resolution Rapid Refresh (HRRR) winds averaged for each scene. We calculated observability for each simulated training scene. Then, we fitted a logistic regression on the simulated scenes.

https://doi.org/10.5194/egusphere-2026-115
Preprint. Discussion started: 3 February 2026

2.7 MAIRX Steady State Emissions Distribution

In the summer of 2023, MethaneAIR flew the MAIRX observation campaign. It covered ∼80% of the oil and gas production in the continental United States (Warren et al. (2024)). Figure 2 shows the MAIRX targets over the Permian and contiguous United States. Plumes were detected via the wavelet and divergence integral methods, and their emission rates quantified by divergence integral (Chulakadabba et al. (2023); Warren et al. (2024)). The emissions distribution was calculated following the ergodic, or steady state assumption (Sherwin et al. (2024)). The steady state assumption posits a constant underlying distribution of plumes, which can be approximated given enough samples. This will produce distributions that do not take source persistence into account. In addition to CH_4 plumes, MethaneAIR also observes regional XCH_4 gradients, which can be used to infer dispersed emissions. Dispersed emissions can be thought of as the regional XCH_4 enhancement due to the combination of plumes too small to be detected as a discrete sources and larger plumes that have spread out after the source has stopped emitting. We quantify these emissions using an inverse method that combines gridded area enhancements with an atmospheric transport model, Stochastic Time Integrated Lagrangian Transport (Lin et al. (2003); MacKay et al. (2025)).

We apply our analysis of the effects of P_d on inferred emissions distributions to the example of the Permian Basin. We took the average dispersed emissions estimate of all the valid scenes for the Permian Basin. The total emissions were defined as the sum of all plume and dispersed emissions. The emissions distribution was defined as the fraction of total emissions associated with plumes of different binned emission rates. To investigate the effects of P_d of different systems on the emissions distribution, we performed Monte Carlo simulation of the analysis. We examined MethaneAIR, MethaneSAT, and a hypothetical satellite with the same spatial resolution as MethaneSAT but worse CH_4 sensitivity, represented by a higher nominal gas concentration noise. We calculated the P_d of these three systems for all observed emission rates for each MAIRX scene, and generated bootstrap samples from MethaneAIR observed plumes. To simulate the observations of MethaneSAT and the hypothetical satellite, each plume was included in the bootstrap sample with probability P_d.

3 Results and Discussion

3.1 Probability of Detection Model

Figure 3 shows the validation comparison for MethaneAIR, using the model trained on the LES simulations. Each point represents image processed controlled release data binned by detection rate. The P_d model works well for the wavelet algorithm applied to MethaneAIR data, but not as well for the divergence integral algorithm. The difficulty for the divergence integral algorithm likely reflects its sensitivity to missing data, which were not present in the training set. This is because the divergence integral algorithm needs intact boxes of XCH_4 pixels of various sizes within the scene, while the wavelet does not. For example, clouds prevent imaging spectrometers from measuring reflected solar light, and leave regions of missing data in real XCH_4 scenes.

https://doi.org/10.5194/egusphere-2026-115
Preprint. Discussion started: 3 February 2026

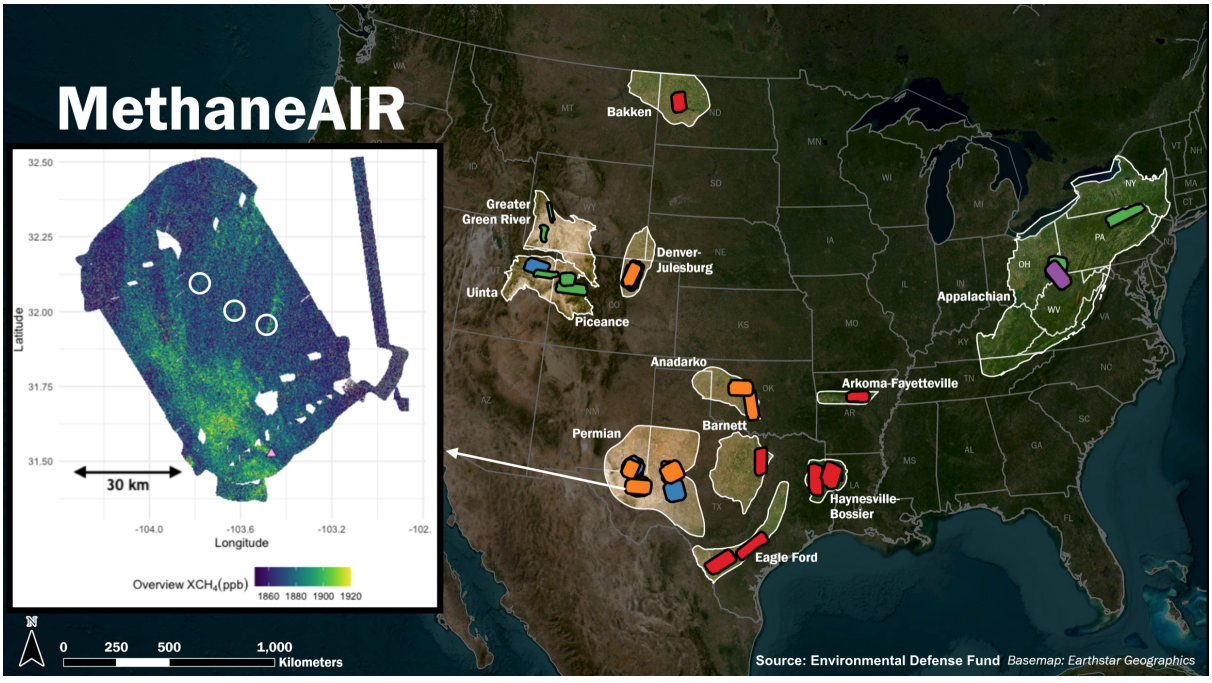

Figure 2. Map of MAIRX targets. Each colored shape is a flight pattern flown by MAIRX. The major oil and gas basins in the contiguous United States are marked. Inset: an example MAIR XCH_4 scene, in which large CH_4 plumes are circled in white. Each colored flight pattern on the map produced an XCH_4 scene like the inset example.

3.2 Observing System Intercomparison

Our probability of detection model quantifies the differences in plume detection capabilities between observing systems and detection algorithms. Figure 4A shows P_d curves modeled for various emission rates and wind speeds for LeakSurveyor™, MethaneAIR, and MethaneSAT. As anticipated, LeakSurveyor's™ lower observation altitude allows it to detect lower emission rate plumes with higher probability than MethaneAIR or MethaneSAT.

In the MAIRX campaign, wind speed controlled P_d more than gas concentration noise. This might not be true for other observing systems with less sensitivity to XCH_4. Although controlled release data for MethaneSAT is not available, g enables prediction of P_d for the divergence integral and wavelet algorithms applied to MethaneSAT scenes. The predicted difference in P_d between MethaneAIR and MethaneSAT is relatively small at low wind speeds compared to high wind speeds.

Because observability normalizes for all observing system features apart from the algorithm, P_d curves in observability space can be used to compare the skill of plume detection algorithms. Figure 4B shows the P_d curves from three different plume detection algorithms. These curves are fitted using simulated XCH_4 scenes (divergence integral and wavelet) and controlled release trials (Insight M). The wavelet algorithm performs better on simulated plumes than the divergence integral. When applied to scenes from the MAIRX campaign, the wavelet algorithm also found more plumes and more low emission rate

https://doi.org/10.5194/egusphere-2026-115
Preprint. Discussion started: 3 February 2026

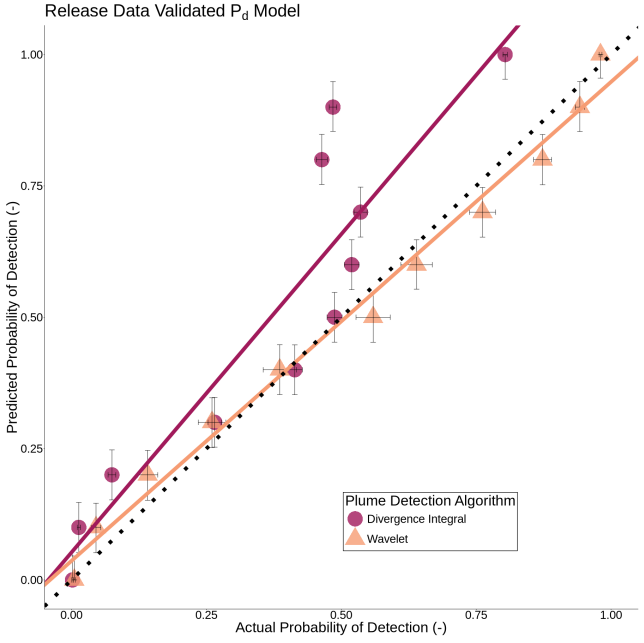

Figure 3. Validation of the probability of detection model using multiplexed affected release plumes and two detection algorithms: divergence integral and wavelet. Each point represents the binned model predicted detection rate (x-axis) compared with the true probability of detection (y-axis). Uncertainty estimates are derived from the binomial central limit theorem. The dotted 1:1 line represents perfect agreement between model predicted and validation P_d. Points above the dotted line represent the model overestimating the probability of detection. The thin colored lines are the best fit lines for each of the detection algorithms. The divergence integral algorithm's best fit line has a slope of 1.22, an intercept of 0.05, and an adjusted R^2 of 0.83. The wavelet algorithm's best fit line has a slope of 0.91, an intercept of 0.36, and an adjusted R^2 of 0.99.

plumes. The Insight M algorithm and controlled release XCH_4 images are proprietary, and we were not able to fit a P_d model to simulated plumes like we were for the divergence integral and wavelet. However, by calculating the observability of the controlled release plumes, we are able to compare the divergence integral, wavelet, and Insight M algorithms. Proprietary Insight M plume detection algorithms are slightly more skillful than the divergence integral and wavelet, independent of the lower observation altitude of Insight M XCH_4 images. The Insight M probability of detection curve has much higher uncertainty than the other algorithms' curves because it is derived from ∼100 controlled release scenes rather than ∼80,000 simulated scenes. Ideally, Insight M images and algorithms would be available for testing. However, our method offers the next best alternative to isolate the effects of detection algorithm, spectrometer, and altitude on P_d.

3.3 MAIRX Steady State Emissions Distribution

Figure 5 shows the observed cumulative emissions distributions for MAIRX, and distributions from simulated observations from MethaneSAT and a hypothetical satellite with the same spatial resolution as MethaneSAT but lower XCH_4 sensitivity.

https://doi.org/10.5194/egusphere-2026-115
Preprint. Discussion started: 3 February 2026

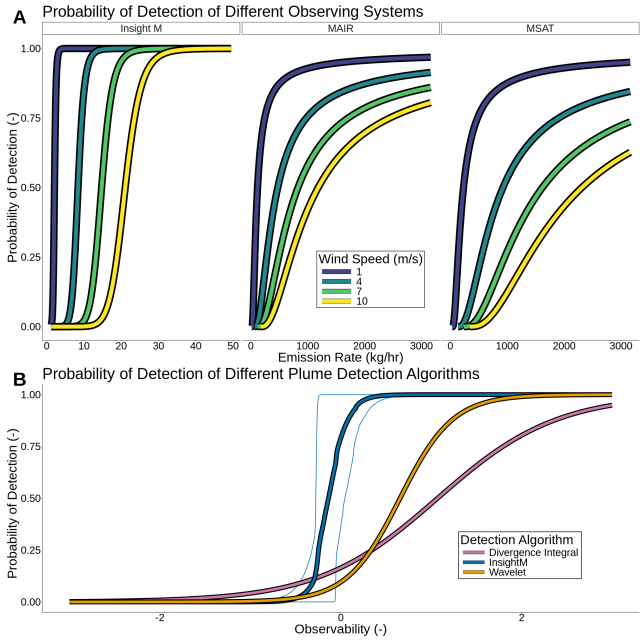

Figure 4. A: Intercomparison of probability of detection between different observing systems (MethaneAIR, MethaneSAT, Insight M) for a range of emission rates and wind speeds. Gas concentration noise was set to the system average for controlled release scenes (MethaneAIR, LeakSurveyor™) or a sample of observational scenes (MethaneSAT). For MethaneAIR and MethaneSAT, the reported P_d is for the wavelet algorithm. **B**: P_d curves for divergence integral, wavelet, and proprietary LeakSurveyor algorithm in observability space. Thick lines are the mean and thin lines are the 95% CI inferred via bootstrap.

Table 2. Fraction of Total Permian Emissions Due to Small and Large Plumes, and Dispersed Emissions, During MAIRX.

System	P_d weighting	≤500 kg/hr	>500 kg/hr	Dispersed
MethaneAIR	No	1% (0%, 2%)	43% (12%, 63%)	56% (39%, 72%)
MethaneAIR	Yes	3% (1%, 5%)	43% (13%, 51%)	55% (38%, 71%)
MethaneSAT	No	3% (1%, 3%)	43% (13%, 62%)	55% (39%, 71%)
MethaneSAT	Yes	3% (1%, 3%)	42% (13%, 61%)	55% (38%, 71%)
Hypothetical Satellite	No	0% (0%, 0%)	30% (0%, 54%)	70% (49%, 91%)
Hypothetical Satellite	Yes	1% (0%, 7%)	40% (0%, 63%)	59% (41%, 76%)

https://doi.org/10.5194/egusphere-2026-115
Preprint. Discussion started: 3 February 2026

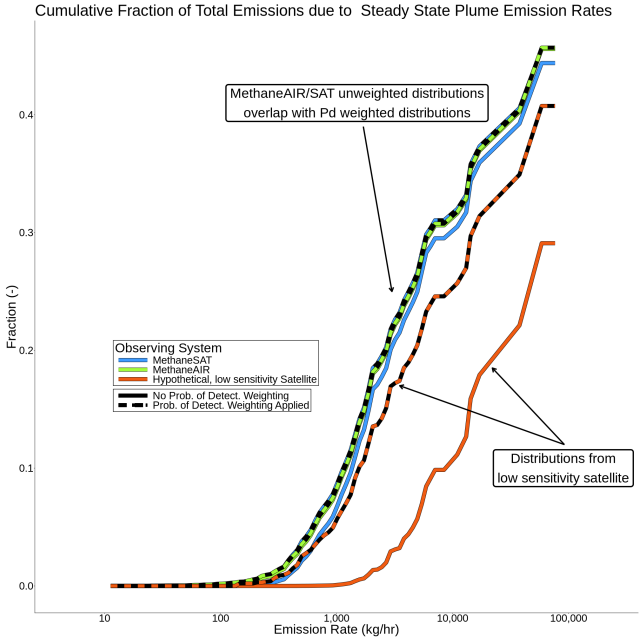

Figure 5. Steady state cumulative fractional contributions of events of different emission rates observed in the Permian, during MAIRX. Distributions are colored to indicate observing system. Dashed distributions include P_d weighting, solid distributions do not. For uncertainties, see Table A1.

Each system has two observed emission distributions, one with P_d weighting (dashed) and one without (solid). Figure B1 shows how including a P_d reduces the heaviness of the tail of the emission rate distribution. Due to heavy tailed oil and gas emissions distributions, the value of an accurate model of the probability of detection increases with higher detection thresholds.

Table A1 contains the fraction of total emissions attributed to plumes <500 kg/hr, plumes >500 kg/hr, and dispersed emissions, for each observing system. The dispersed emissions represent CH_4 from current plumes too small to be detected and from extinct plumes that have dispersed. For MethaneAIR, there is close agreement between the cumulative distribution with P_d weighting and the one without, indicating that measurements capture the most significant plumes. The P_d term shifts a small fractional contribution of $\sim$1% from dispersed emissions to plumes <500 kg/hr (Table A1). These results indicate that for the Permian, an observing system with a nominal P_d inflecting in the hundreds of kg/hr CH_4 range is sufficient for characterizing the small population of plumes >500 kg/hr that control total plume associated emissions. This assessment is contingent on well constrained dispersed emissions—in this case, generated by MethaneAIR.

MethaneSAT has coarser spatial resolution than MethaneAIR, but higher XCH_4 sensitivity, resulting in a lower average scene gas concentration noise. It retains the ability to detect moderate plumes, inflecting at $\sim$500 kg/hr compared to MethaneAIR's $\sim$200 kg/hr at 5 m/s wind speed (Figure 4A). This difference in P_d is not enough for P_d to materially affect the inferred contribution of emission rates >500 kg/hr to total emissions.

https://doi.org/10.5194/egusphere-2026-115
Preprint. Discussion started: 3 February 2026

We also analyze a hypothetical satellite with lower XCH_4 sensitivity to show a case where the P_d term is important. In Figure 5, the distribution produced by the hypothetical lower sensitivity instrument (orange) diverges from those produced by the higher sensitivity instruments (yellow and blue). However, the P_d weighted distribution (dashed orange) is more similar to the "ground truth" from MethaneAIR (yellow), indicating that the P_d term recovers most of the missed emissions from both large and small plumes (Table A1). However, these P_d weighted estimates have much wider CI's, due to fewer plume observations. Pandey et al. (2024) also note P_d controlled transfer between dispersed and plume emissions. Analysis of low XCH_4 sensitivity systems is relevant to projects attempting to detect CH_4 plumes with multispectral satellites, which may only have one radiation band with CH_4 absorption, such as Rouet-Leduc and Hulbert (2024).

Our estimated emissions distributions differ from other analysis of MethaneAIR plume observations of the Permian (Warren et al. (2024)). We find a higher fraction of total emissions due to plumes. One explanantion is that Warren et al. (2024) only used plumes detected by the divergence integral, while we included both wavelet and divergence integral detected plumes. Additionally, Warren et al. (2024) use a persistence weighting approach (Cusworth et al (2021)). Persistence weighting accounts for intermittency of sources by multiplying their steady state emission rate by $\frac{N_e}{N_o}$, where N_e is the number of times the source was observed emitting and N_o is the number of times it was observed. This would decrease the inferred fraction of total emission from plumes. There are large uncertainties in the steady state fraction of emissions attributable to large plumes (Table A1). These uncertainties reflect the importance of a good assessment of the duration and arrival intensity of ephemeral plumes.

In our consideration of the effect of P_d on emissions distributions, we adopted the steady state assumption. It is not clear how many repeat observations of the same domain are needed for a steady state model to recover the true emissions distribution. In light of difference with emissions distributions that incorporate persistence weighting (Warren et al. (2024)), a more complex model of intermittent plumes may be justified.

4 Conclusions

Probability of detection is critical for interpretation of observations of plumes and inference of emissions distributions. Our approach to modeling P_d can dispense with controlled release data, which makes it is particularly relevant for satellites and for designing future missions. This approach could also be used to predict the probability of detection of plumes of gasses other than CH_4, such as carbon dioxide plumes emitted by combustion power plants. Missions that seek to constrain the fractional contribution of emission rates $>$500 kg/hr should prioritize observational coverage and capturing regional diffuse emissions. Capturing dispersed emissions is equivalent for this objective to discerning small plumes (Table A1). MethaneAIR and MethaneSAT are capable of detecting small enough plumes to effectively probe the heavy tailed emission rate distributions found in the Permian, as well other North American basins.

Code availability. See git@github.com:emanninen/probabilities_of_detection_of_methane_plumes_by_remote_sensing_code.git

https://doi.org/10.5194/egusphere-2026-115
Preprint. Discussion started: 3 February 2026

Table A1. Fitted Logistic Regression Parameters for MethaneAIR, MethaneSAT, and Insight M

Algorithm	Intercept (standard error)	Slope (standard error)
Divergence Integral	-1.62 (0.02)	1.52 (0.02)
Wavelet	-2.26 (0.04)	3.44 (0.05)
Insight M	1.18 (0.79)	9.9 (3.36)

Data availability. MethaneAIR data can be found for MAIR at https://www.eol.ucar.edu/field_projects/methaneair, for MAIR-E, at https://www.eol.ucar.edu/field_projects/mair-e, and for MAIRX on Google Earth Engine at https://developers.google.com/earth-engine/datasets/catalog/EDF_MethaneSAT_MethaneAIR_L4point.

https://doi.org/10.5194/egusphere-2026-115
Preprint. Discussion started: 3 February 2026

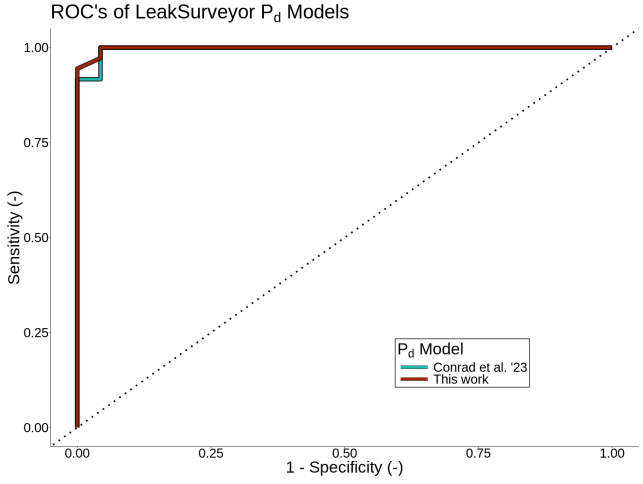

Figure A1. Receiver Operator Curve of fitted P_d models tested on controlled release data. X-axis is the true positive rate, or sensitivity, y-axis is the false positive rate, or the complement of specificity. Teal curve is for the model fitted by Conrad et al. (2023). Red curve is for the model fitted in this work.

Figure A1 shows receiver operator curves (ROC) generated by predicting P_d of LeakSurveyor's controlled release detection results from the 2022 controlled release using our methodology and Conrad et al. (2023)'s P_d model fit with 2021 controlled release data. Our model has more area under the ROC than Conrad et al. (2023)'s, indicating more predictive skill. However, this difference is not statistically significant. This is because we only are able to use $\sim$100 controlled release overpasses from the 2022 Arizona controlled release for comparison of the two models. With more data, the two ROC's may diverge further. The Conrad et al. (2023) model is fit to the observing conditions of the 2021 controlled release experiment. Additionally, it was fit at the 2021 900 m observing altitude, while in 2022, they flew at a much lower altitude, resulting in a smaller native pixel area and higher P_d's. Conrad et al. (2023)'s model does not have a term to adjust the observing altitude and thus pixel area and gas concentration noise.

Figure B1 shows the Cumulative Distribution Functions (CDF) of emission rates detected by the two MethaneAIR plume detection algorithms. Two emission rate distributions are presented, one with a P_d weighting term defined as $N_{weighted} = N_{observed}/P_d$ for a number of plumes N. For the CDF's without P_d weighting, the wavelet's higher probability to detect low emission rate plumes results in a less heavy tailed distribution. Including P_d weighting results in less heavy tailed distributions for both algorithms. However, the two P_d weighted CDF's still diverge, indicating that the P_d weighting did not fully recover possible distribution. This is likely due to the overestimate of P_d for the divergence integral algorithm (Figure 3).

https://doi.org/10.5194/egusphere-2026-115
Preprint. Discussion started: 3 February 2026

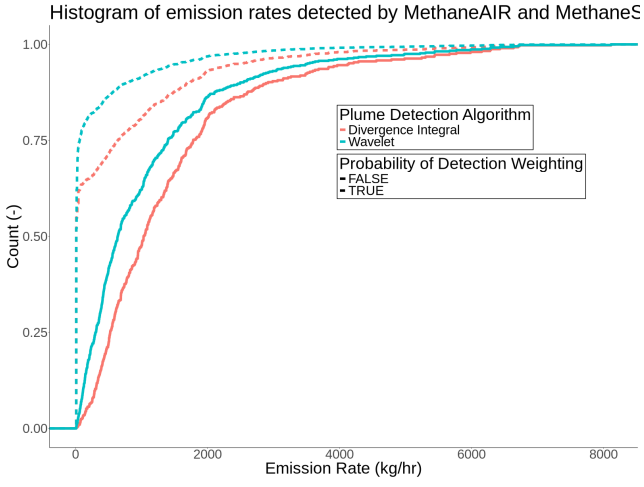

Figure B1. A: Empirical CDF of emission rates. The x-axis is emission rate q; the y-axis shows $F(q) = P(q_{obs} < q)$. Two pairs of curves are shown for each operational detection algorithm (indicated by color). Solid lines do not include P_d weighting, dashed lines include P_d weighting. For N plumes, $N_{weighted} = N_{observed}/P_d$.

https://doi.org/10.5194/egusphere-2026-115
Preprint. Discussion started: 3 February 2026

Author contributions. EM, JC and SW planned the study. EM did the statitical analyses. EM wrote the manuscript. AC performed plume simulations. AC, ZZ and MS developed plume detection algorithms. HK formatted Insight M controlled release data. SR, CCM, BL, KS, XL, and JF developed XCH_4 retrieval algrothims. EK, JB, EW, and JB developed area emissions inversions. JS and JH analyzed and calibrated MAIR spectrometers.

Competing interests. The authors declare no competing interests

Acknowledgements. Funding for MethaneSAT and MethaneAIR was provided in part by Arnold Ventures, The Audacious Project, Ballmer Group, Bezos Earth Fund, The Children's Investment Fund Foundation, Heising-Simons Family Fund, King 385 Philanthropies, Robertson Foundation, Skyline Foundation and Valhalla Foundation. For a more complete list of funders, please visit www.methanesat.org. Seed funding for development of the MethaneAIR sensor was provided by Harvard University, the Smithsonian Institution, and the Stonington Fund. Flights of the NSF Gulfstream V (RF04 - RF08) were supported by the National Science Foundation (NSF1856426 (EAGER)). TUM authors were partially funded by EU projects "PAUL" under Grant 101037319 and "CoSense4Climate" under Grant 101089203. The authors thank David Miller for his contributions to the MethaneAIR and MethaneSAT programs. We thank Rachel Oshiro for help with LaTeX formatting.

https://doi.org/10.5194/egusphere-2026-115
Preprint. Discussion started: 3 February 2026

References

Akaike, H.: Information Theory and an Extension of the Maximum Likelihood Principle, in: Breakthroughs in Statistics, pp. 610–624, Springer, New York, NY, ISBN 978-1-4612-0919-5, https://doi.org/10.1007/978-1-4612-0919-5_38, 1992.

Ayasse, A. K., Cusworth, D. H., Howell, K., O'Neill, K., Conrad, B. M., Johnson, M. R., Heckler, J., Asner, G. P., and Duren, R.: Probability of Detection and Multi-Sensor Persistence of Methane Emissions from Coincident Airborne and Satellite Observations, Environmental Science & Technology, 58, 21 536–21 544, https://doi.org/10.1021/acs.est.4c06702, 2024.

Bruno, J. H., Jervis, D., Varon, D. J., and Jacob, D. J.: U-Plume: Automated Algorithm for Plume Detection and Source Quantification by Satellite Point-Source Imagers, Atmospheric Measurement Techniques, 17, 2625–2636, https://doi.org/10.5194/amt-17-2625-2024, 2024.

Chan Miller, C., Roche, S., Wilzewski, J. S., Liu, X., Chance, K., Souri, A. H., Conway, E., Luo, B., Samra, J., Hawthorne, J., Sun, K., Staebell, C., Chulakadabba, A., Sargent, M., Benmergui, J. S., Franklin, J. E., Daube, B. C., Li, Y., Laughner, J. L., Baier, B. C., Gautam, R., Omara, M., and Wofsy, S. C.: Methane Retrieval from MethaneAIR Using the CO_2 Proxy Approach: A Demonstration for the Upcoming MethaneSAT Mission, Atmospheric Measurement Techniques, 17, 5429–5454, https://doi.org/10.5194/amt-17-5429-2024, 2024.

Chulakadabba, A., Sargent, M., Lauvaux, T., Benmergui, J. S., Franklin, J. E., Chan Miller, C., Wilzewski, J. S., Roche, S., Conway, E., Souri, A. H., Sun, K., Luo, B., Hawthrone, J., Samra, J., Daube, B. C., Liu, X., Chance, K., Yang, L., Gautam, R., Omara, M., Rutherford, J. S., Sherwin, E. D., Brandt, A., and Wofsy, S. C.: Methane Point Source Quantification Using MethaneAIR: A New Airborne Imaging Spectrometer, Atmospheric Measurement Techniques, 16, 5771–5785, https://doi.org/10.5194/amt-16-5771-2023, 2023.

Conrad, B. M., Tyner, D. R., and Johnson, M. R.: Robust Probabilities of Detection and Quantification Uncertainty for Aerial Methane Detection: Examples for Three Airborne Technologies, Remote Sensing of Environment, 288, 113 499, https://doi.org/10.1016/j.rse.2023.113499, 2023.

Conway, E. K., Souri, A. H., Benmergui, J., Sun, K., Liu, X., Staebell, C., Chan Miller, C., Franklin, J., Samra, J., Wilzewski, J., Roche, S., Luo, B., Chulakadabba, A., Sargent, M., Hohl, J., Daube, B., Gordon, I., Chance, K., and Wofsy, S.: Level0 to Level1B Processor for MethaneAIR, Atmospheric Measurement Techniques, 17, 1347–1362, https://doi.org/10.5194/amt-17-1347-2024, 2024.

El Abbadi, S. H., Chen, Z., Burdeau, P. M., Rutherford, J. S., Chen, Y., Zhang, Z., Sherwin, E. D., and Brandt, A. R.: Technological Maturity of Aircraft-Based Methane Sensing for Greenhouse Gas Mitigation, Environmental Science & Technology, 58, 9591–9600, https://doi.org/10.1021/acs.est.4c02439, 2024.

Gaudet, B. J., Lauvaux, T., Deng, A., and Davis, K. J.: Exploration of the Impact of Nearby Sources on Urban Atmospheric Inversions Using Large Eddy Simulation, Elementa: Science of the Anthropocene, 5, 60, https://doi.org/10.1525/elementa.247, 2017.

Hüpfel, M., Yu. Kobitski, A., Zhang, W., and Nienhaus, G. U.: Wavelet-Based Background and Noise Subtraction for Fluorescence Microscopy Images, Biomedical Optics Express, 12, 969–980, https://doi.org/10.1364/BOE.413181, 2021.

Laughner, J. L., Roche, S., Kiel, M., Toon, G. C., Wunch, D., Baier, B. C., Biraud, S., Chen, H., Kivi, R., Laemmel, T., McKain, K., Quéhé, P.-Y., Rousogenous, C., Stephens, B. B., Walker, K., and Wennberg, P. O.: A New Algorithm to Generate a Priori Trace Gas Profiles for the GGG2020 Retrieval Algorithm, Atmospheric Measurement Techniques, 16, 1121–1146, https://doi.org/10.5194/amt-16-1121-2023, 2023.

Lin, J. C., Gerbig, C., Wofsy, S. C., Andrews, A. E., Daube, B. C., Davis, K. J., and Grainger, C. A.: A Near-Field Tool for Simulating the Upstream Influence of Atmospheric Observations: The Stochastic Time-Inverted Lagrangian Transport (STILT) Model, Journal of Geophysical Research: Atmospheres, 108, https://doi.org/10.1029/2002JD003161, 2003.

https://doi.org/10.5194/egusphere-2026-115
Preprint. Discussion started: 3 February 2026

MacKay, K., Benmergui, J., Williams, J. P., Omara, M., Himmelberger, A., Sargent, M., Warren, J. D., Miller, C. C., Roche, S., Zhang, Z., Guanter, L., Wofsy, S., and Gautam, R.: Assessment of Methane Emissions from US Onshore Oil and Gas Production Using MethaneAIR Measurements, preprint, https://doi.org/10.5194/egusphere-2025-3008, 2025.

Roger, J., Guanter, L., and Gorroño, J.: Assessing the Detection of Methane Plumes in Offshore Areas Using High-Resolution Imaging Spectrometers, https://doi.org/10.5194/egusphere-2025-1917, 2025.

Rouet-Leduc, B. and Hulbert, C.: Automatic Detection of Methane Emissions in Multispectral Satellite Imagery Using a Vision Transformer, Nature Communications, 15, 3801, https://doi.org/10.1038/s41467-024-47754-y, 2024.

Sherwin, E. D., Yuanlei, C., Ravikumar, A. P., and Brandt, A. R.: Single-Blind Test of Airplane-Based Hyperspectral Methane Detection via Controlled Releases, Elementa: Science of the Anthropocene, 9, https://doi.org/10.1525/elementa.2021.00063, 2021.

Sherwin, E. D., Rutherford, J. S., Chen, Y., Aminfard, S., Kort, E. A., Jackson, R. B., and Brandt, A. R.: Single-Blind Validation of Space-Based Point-Source Detection and Quantification of Onshore Methane Emissions, Scientific Reports, 13, 3836, https://doi.org/10.1038/s41598-023-30761-2, 2023.

Sherwin, E. D., Rutherford, J. S., Zhang, Z., Chen, Y., Wetherley, E. B., Yakovlev, P. V., Berman, E. S. F., Jones, B. B., Cusworth, D. H., Thorpe, A. K., Ayasse, A. K., Duren, R. M., and Brandt, A. R.: US Oil and Gas System Emissions from Nearly One Million Aerial Site Measurements, Nature, 627, 328–334, https://doi.org/10.1038/s41586-024-07117-5, 2024.

Staebell, C., Sun, K., Samra, J., Franklin, J., Chan Miller, C., Liu, X., Conway, E., Chance, K., Milligan, S., and Wofsy, S.: Spectral Calibration of the MethaneAIR Instrument, Atmospheric Measurement Techniques, 14, 3737–3753, https://doi.org/10.5194/amt-14-3737-2021, 2021.

Varon, D. J., Jacob, D. J., McKeever, J., Jervis, D., Durak, B. O. A., Xia, Y., and Huang, Y.: Quantifying Methane Point Sources from Fine-Scale Satellite Observations of Atmospheric Methane Plumes, Atmospheric Measurement Techniques, 11, 5673–5686, https://doi.org/10.5194/amt-11-5673-2018, 2018.

Warren, J. D., Sargent, M., Williams, J. P., Omara, M., Miller, C. C., Roche, S., MacKay, K., Manninen, E., Chulakadabba, A., Himmelberger, A., Benmergui, J., Zhang, Z., Guanter, L., Wofsy, S., and Gautam, R.: Sectoral Contributions of High-Emitting Methane Point Sources from Major U.S. Onshore Oil and Gas Producing Basins Using Airborne Measurements from MethaneAIR, EGUsphere, pp. 1–22, https://doi.org/10.5194/egusphere-2024-3865, 2024.